
The Space Congress® Proceedings

1967 (4th) Space Congress Proceedings

Apr 3rd, 12:00 AM

# Experimental Investigation at M-20 of the Longitudinal Aerodynamic Characteristics, Pressure and Heat Transfer Distribution on a 50° Semivertex Angle Sphere-Cone

S. Steinberg
*Flight Dynamics Department, Martin Company, Baltimore, Maryland*

A. R. Flesjer
*Flight Dynamics Department, Martin Company, Baltimore, Maryland*

# EXPERIMENTAL INVESTIGATION AT M = 20 OF THE LONGITUDINAL AERODYNAMIC CHARACTERISTICS, PRESSURE AND HEAT TRANSFER DISTRIBUTION ON A 50° SEMIVERTEX ANGLE SPHERE-CONE

By S. Steinberg and A. R. Flesher

Flight Dynamics Department, Martin Company, Baltimore, Maryland

## INTRODUCTION

As part of continuing generalized overall space exploration studies, the Martin Company Space Exploration Group has been engaged in detailed study of the conceptual design of systems and configurations which ultimately would lead to development of a configuration suitable both for Mars atmosphere entry and landing an instrumented payload on the planet's surface. A significant aspect of these Voyager Program Studies encompassed an experimental program devoted to obtaining detailed data concerning the aerodynamic characteristics, heat transfer, and pressure distributions on high-drag configurations at Mach numbers typical of atmospheric entry. One of our most comprehensive experimental efforts associated with the aerodynamics of atmospheric entry included investigations on a 50° semivertex angle sphere-cone equipped with varied afterbody shapes (Fig. 1). This configuration is the subject of this paper. It was specifically selected because it is representative of an applicable Voyager configuration and is a simple enough shape to permit comparison of the experimental results with those obtained by theoretical study.

The facility utilized for these investigations was the Martin Company's 25-in. Arc Heated Wind Tunnel [1] located at Middle River, Maryland. All the tests were conducted at a nominal Mach number of 20 in dry nitrogen, and data were obtained at environmental conditions which closely simulated portions of a typical de-orbit trajectory of the Voyager Lander configuration as exemplified in Fig. 2. The trajectories superimposed on these plots are de-orbit mode trajectories into the Martian atmospheres commonly known as VM-7 and VM-8, which are based upon the Mariner IV occultation experiment.

## THE MODELS

The models used in this investigation were of two distinct types. One type was designed specifically for the heat transfer and pressure test phase of the program and incorporated provisions for both the heat transfer and pressure instrumentation within the confines of the steel walls and the model cavity. The other type of models was designed solely for the force and moment tests and consisted basically of thin walled fiberglass cloth molded models embodying an aluminum honeycomb bulkhead used both as an outer shell stiffener and as a strain-gage balance support member. The internal body of the models was comprised of foaming plastic. To meet the angle of attack requirements of 0° to 180°, it was necessary to provide 5 models of each configuration. These force models were of lightweight construction to minimize inertia loads on the strain gage balance signal outputs. The dimensional details of the models are given in Fig. 1; photographs of the models and of a typical mounting in the tunnel are presented in Fig. 3.

## INSTRUMENTATION

Pressure instrumentation. The pressure measurements were made with variable reluctance wafer-type pressure transducers. In general, the overall system accuracy based upon repeatability of data is within ± 5%. The transducers are calibrated on a daily basis during the active part of the test period. The pressure instrumentation within the model numbered 15 transducers distributed as shown in Fig. 1.

Heat transfer gages. The heat transfer measurements were made with calorimeter type transducers which originally were designed specifically for small models. New miniature gages were made especially for this investigation. These minute gages consist of a 1/16-in. O. D. body encompassing a thin silver disc as the calorimeter with a chromel-constantan thermocouple spot welded to its rear surface. The disc thickness is dependent on the heat input and, in general, varies from 0. 003 to 0. 010 in. An enlarged schematic diagram of a typical gage is presented in Fig. 4. Due to its relative size and the problems involved in the use of this type of transducer, the calorimeter is not an inherently accurate device when compared with pressure or force measuring instruments. However, by careful calibrations and interpretation of the calibration curves and by judicious fairing of the actual data, it is believed that the data are accurate to within 15% and are in keeping with the general accuracy of heat transfer measurements in such facilities. Sixteen such gages were installed for the tests, and their locations are also shown in Fig. 1. Reference 2 presents a complete description of the heat gages and their calibration.

Reference probe. A 15° semivertex angle sphere-cone probe is mounted in the tunnel during each test shot to provide a reference stagnation heat transfer rate at any instant. These data are used to define the test section conditions and also to infer a model stagnation heat transfer rate when the model is at an angle of attack. This probe is equipped with a stagnation heat transfer gage and three additional gages located on the cone. It can be seen in the installation photograph, Fig. 3.

Strain gage balance. The longitudinal force and moment coefficient data were obtained through utilization of a standard 1/2 in. three-component strain gage balance. The normal and axial force component measurements are the most accurate, and multiple test runs have shown repeatability within ± 5. 5%. The calibration accuracy is within 1% of full scale outputs on all components. However, the pitching moment data have the greatest inaccuracy in that the balance pitch center in some instances is quite removed from the center of the model load. This is unavoidable since the model is relatively short with respect to the balance length. In addition, since several model-sting arrangements were required to encompass an angle of attack range of 180°, certain arrangements were more favorable than were others from the viewpoint of pitching moment accuracy.

Each of the three types of instrumentation used in this investigation yielded outputs that were recorded in the same manner, that is, the signal was amplified by a 20-kc carrier amplifier before being recorded by

a high speed oscillograph. In the case of the strain gage balance, the inertia effects of the model-support system were minimized by the insertion of appropriate notch filters.

## TESTS

Pressure and heat transfer tests. As previously mentioned and as shown in Fig. 1, the pressure and heat transfer model incorporated 17 minute heat transfer gages and 15 pressure orifice locations, each in individual diametrically opposing 90° segments of the model. This was done in order that windward pressure data might be obtained simultaneously with leeward heat transfer data and vice versa. In this manner, an angle range encompassing $\pm$ 90° would provide the required data. A total of 20 such test shots was made including repeat runs.

Longitudinal force tests. This series of runs included tests and repeats covering an angle of attack range of 0 to 180° on the model configurations noted both in Fig. 1 and the applicable photographs of Fig. 3. In all, 27 shots were made on the basic model with the flat back, 15 shots on the configuration with the 60° semivertex cone angle afterbody and 13 shots on the configuration having the 30° semivertex cone angle afterbody.

All tests were made at a nominal Mach number of 20 at stagnation temperatures of about 3000° K. The Reynolds number varied from shot to shot but generally was about $6.5 \times 10^4$ based upon the 4.5-in. base diameter of the model.

The data for all phases of this investigation were reduced by the special computer programs of Ref. 3. The mathematical methods of Ref. 4 were used to derive the test section environment for all the tunnel runs.

## DISCUSSION OF RESULTS

### Longitudinal Aerodynamic Characteristics

The longitudinal aerodynamic characteristics in the wind axis system are plotted in Figs. 5 through 7 for the three configurations. Figure 5 presents the data for the basic configuration with the flat base, while Figs. 6 and 7 similarly present the data for the 60° and 30° afterbodies, respectively. It should be noted that only the actual data points are plotted thereon with no specific fairing attempted. Instead, modified Newtonian curves based upon the data of Ref. 5 are presented so that test and theory may be easily compared. The modification is based upon using a pressure coefficient of 1.81 instead of the value of 2.00 used in the reference. The value of 1.81 is based upon the nominal test section environmental conditions. In addition, afterbody effects were added to the Ref. 5 data as required so that the entire angle range might appropriately be included. The figures show that the general agreement of the force coefficient data with the calculated Newtonian values is quite good. Differences between Newtonian values and the experimental data are attributable to a combination of both viscous induced effects and conical pressure level differences not present in the Newtonian theory. To illustrate these differences, one can examine the 0 to 180° points of each configuration. Comparing the $\alpha$ point of Fig. 5 with the 180° data of Figs. 6 and 7 shows the greatest departure of drag coefficient, $C_D$, from the Newtonian value to occur for the Fig. 7 configuration. This represents the smallest cone angle and, consequently, the greatest viscous effect. The 60° half cone angle represented by the Fig. 6 configuration shows the Newtonian value to be virtually coincident with the experimental data, indicating a minimum viscous effect. This is also the case for the Fig. 5 data at 180° when the Newtonian constant of 1.80 is attained.

The pitching moment data generally show the greatest departure from the Newtonian values. This is due to both the location of the model center of pressure with respect to the balance electrical center which reduces the accuracy, and to the conical pressure level and viscous induced effects which would cause the model CP to move aft. In general, the experimental data show similar trends with the Newtonian curves up to $\alpha$ of 70° but there is variance in the magnitude. The configuration with the 30° conical afterbody is associated with the most favorable balance center position. Figure 7 shows the smoothest measured data, and similar trends with the Newtonian values are apparent throughout the entire angle of attack range.

### Pressure Data

As noted earlier, and as shown in Fig. 1, the model was instrumented with 15 pressure orifices. Both windward and leeward pressure data were obtained. Figure 8b shows the data of a representative orifice location plotted in terms of pressure ratio versus angle of attack. These data are seen to be consistently smooth, and the point scatter associated with repeat runs is small. On the basis of all the pressure data obtained, and from plots similar to Fig. 8b, the data were crossplotted. Figure 9 presents a typical plot of pressure ratio versus normalized surface distance of orifice for the stagnation line meridian (orifices 2 to 6) at constant angles of attack up to 40°. Superimposed on this plot is the representative Newtonian value level for comparison. The departure from the Newtonian values is evident with the variance being greatest at the lower angles of attack. At an angle of attack of 40°, when the stagnation line meridian is normal to the flow direction, it can be seen that the Newtonian value agrees with the experimental value at a mean value of S/R and is constant for approximately one nose radius on either side of the cone midpoint.

From the plots and crossplots made, contours of constant pressure ratio are presented in Fig. 10 on a semicircular projection of the model for each angle of attack tested. The movement of the peak pressure on the stagnation line is readily apparent as is the subsonic conical pressure ratio encountered over the entire angle range.

### Heat Transfer Data

The instrumentation coverage for obtaining the heat transfer data included a stagnation heat transfer gage and 15 additional gages located identically to the pressure orifices (Fig. 1). Figure 8a presents typical data of one heat gage located in an identical relative position to that previously given for a pressure orifice in Fig. 8b. In this case, the ratio of local to a reference stagnation heat rate has been plotted versus the angle of attack for both windward and leeward angles. The data scatter here is seen to be more pronounced than exists for the pressure data, which is to be expected.

The stagnation heat rate on the model as measured at zero angle of attack was found to be somewhat lower (about 12%) than would be predictable for that nose radius based upon the stagnation rates as measured on a

15° sphere-cone reference probe. This is implied on the basis of three individual runs at $\alpha = 0$, and is perhaps due to the sonic line being positioned at the cone extremity rather than on the spherical nose. The inference is that the 50° cone semivertex angle bluntness has influenced the flow over the spherical nose such that a Newtonian velocity gradient does not exist. Thus, the stagnation heat rate cannot be conventionally converted from the measuring media of the 15° cone reference probe. Due to the uncertainty associated with this effect, the heat transfer rates for this investigation have been normalized by the stagnation of $\dot{q}$ as measured on the nose of the model. On this basis, the value of $\dot{q}/\dot{q}_s$ at $\alpha = 0°$ for the stagnation gage on the model is unity. At angle of attack, and in the absence of a stagnation heat gage, $\dot{q}_s$ was inferred from the 15° cone reference probe utilizing the following equation:

$$\dot{q}_{s_{model}} = 0.88\sqrt{\frac{R_p}{R_N}}\,\dot{q}_{s\ probe}$$

where

$R_P$ and $R_N$ are the nose radii of the probe and model, respectively.

While this procedure is undoubtedly not rigorously correct, it does afford one the opportunity of presenting the data in a consistent manner.

Figure 11 presents a conventional plot of local-stagnation heat rate ratio plotted versus normalized surface distance for the stagnation line windward meridian at several angles of attack. The experimental results are compared with the theory of Stern from Ref. 6. It is seen that at 0 and 10° angles of attack, the comparison is quite reasonable, but that the experimental results at $\alpha = 30°$ are considerably higher than the theory.

A procedure similar to that utilized for the pressure data was also performed for the heat transfer data. That is, crossplots of the data were used to make contours of heat transfer ratio on a projected view of the model surface at each test angle of attack from 0 to 90°. This is presented in Fig. 12 and is seen to be similar to the pressure contours. Specifically, the stagnation point moves toward the cone extremity with increasing angle of attack, while the $\dot{q}$ ratio decreases since the local stagnation point radius grows larger with increasing $\alpha$.

## CONCLUSIONS

Comprehensive experimental investigations on a 50° semivertex angle cone configuration to obtain pressure, heat transfer and the longitudinal aerodynamic characteristics to angles of attack of 180° indicated the following:

(1) Detailed surface pressure distributions and heat transfer rate data can be simultaneously obtained on relatively small models.

(2) Newtonian aerodynamics can generally be used to predict the force coefficient data of blunt sphere-cone configurations but appears to be less adequate in estimating pitching moment values.

(3) Pressure distribution data show some departure from pure Newtonian values, although the integrated force measurements made closely approximated modified Newtonian values.

(4) Evidence exists that conical bluntness appears to reduce the stagnation heat transfer rate below that which would be conventionally predictable. In particular, cone angles above 50° may not permit analysis where the assumption of Newtonian velocity gradient must be made.

## REFERENCES


1. L. G. Cooper, S. M. Gottlieb, R. Phinney, "The Martin Hot Shot Hypersonic Wind Tunnel," Martin Company ER 12085, November 1964.

2. E. N. Screen, "Instrument Development Report for Hypersonic Heat Transfer Studies, " Martin Company ER 13061, June 1963.

3. A. R. Flesher, "Data Reduction Systems for the Martin Hypersonic Wind Tunnel," Martin Company ER 13427, April 1964.

4. M. Grabau, R. L. Humphrey, W. J. Little, "Determination of Test Section, After Shock, and Stagnation Conditions in Hot Shot Tunnels Using Real Nitrogen at Temperatures from 3000-4000° K," AEDC TN-61-82, July 1961.

5. E. E. Mayo, R. H. Lamb, P. O. Rosmere, "Newtonian Aerodynamics for Blunted Raked-Off Circular Cones and Raked-Off Elliptical Cones," NASA TN-D-2624, May 1965.

6. I. Stern, "Integrated Laminar Heat Transfer in the Windward Plane of Yawed Blunt Cones," AIAA Journal, July 1963.

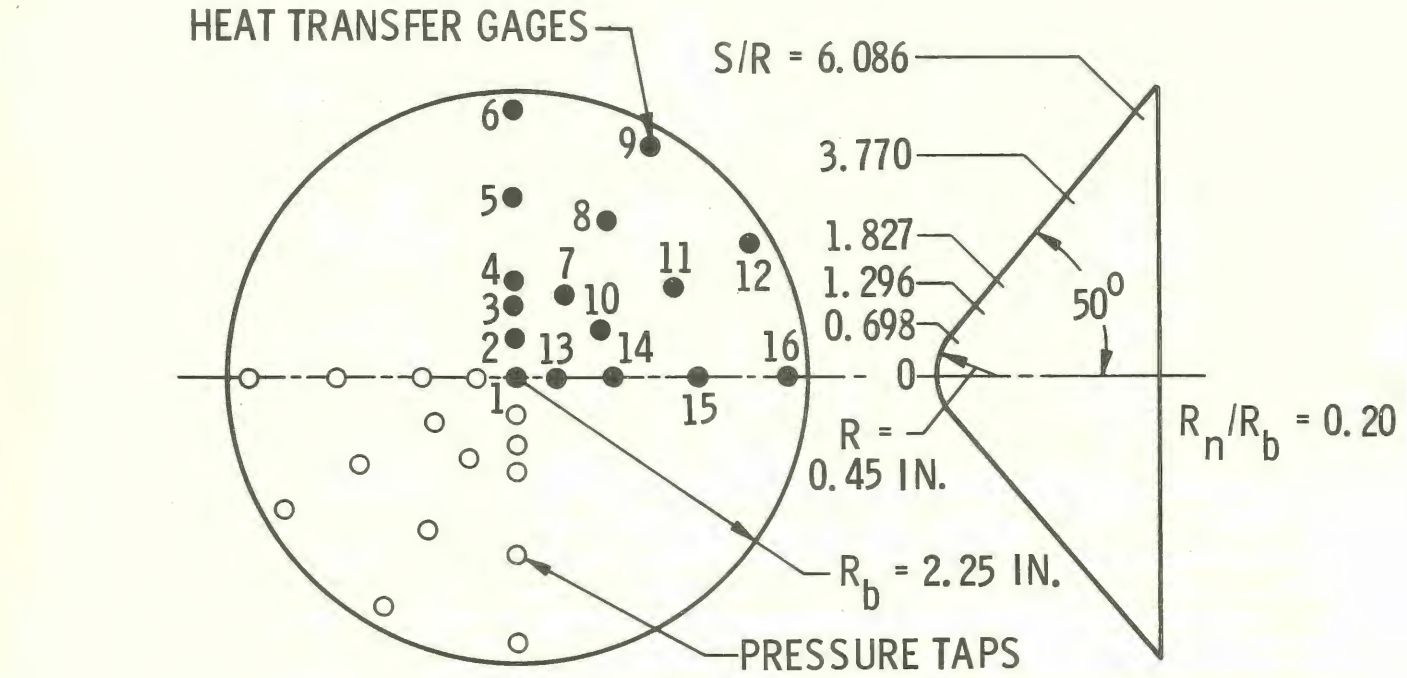


HEAT TRANSFER AND PRESSURE MODEL

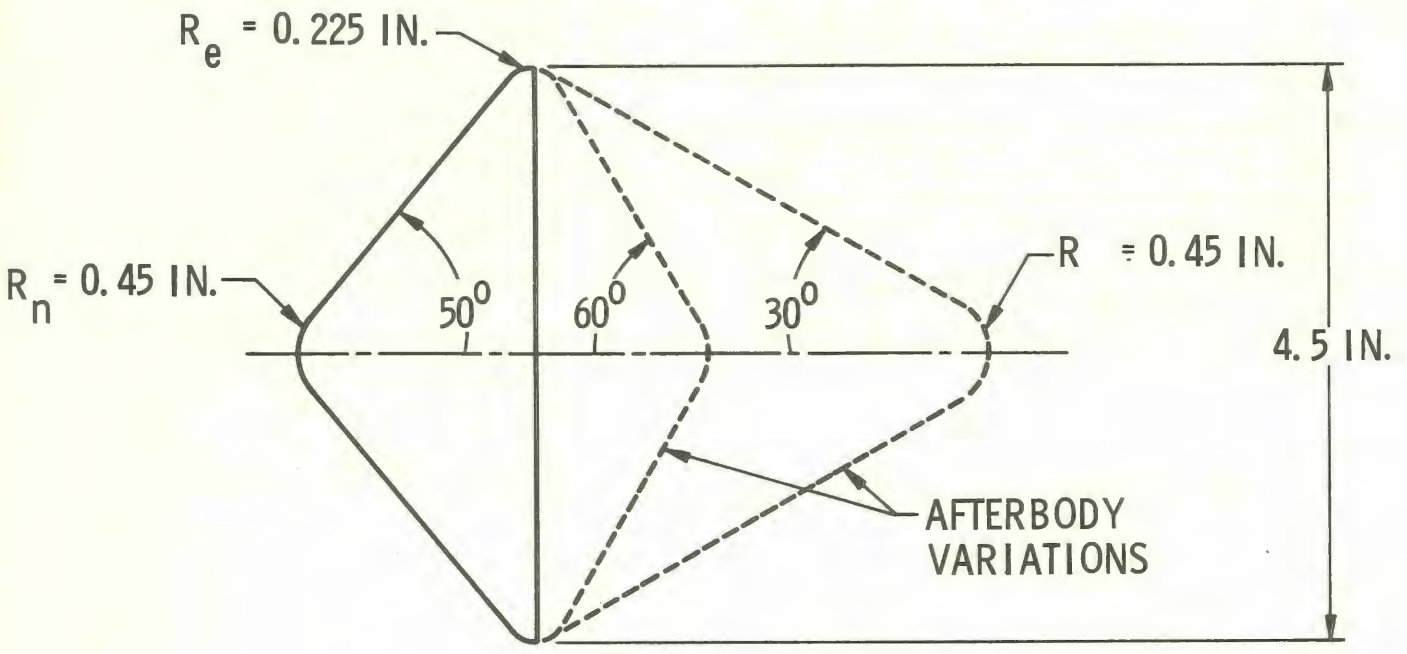


FORCE MODELS

**Figure 1. Model Geometry.**

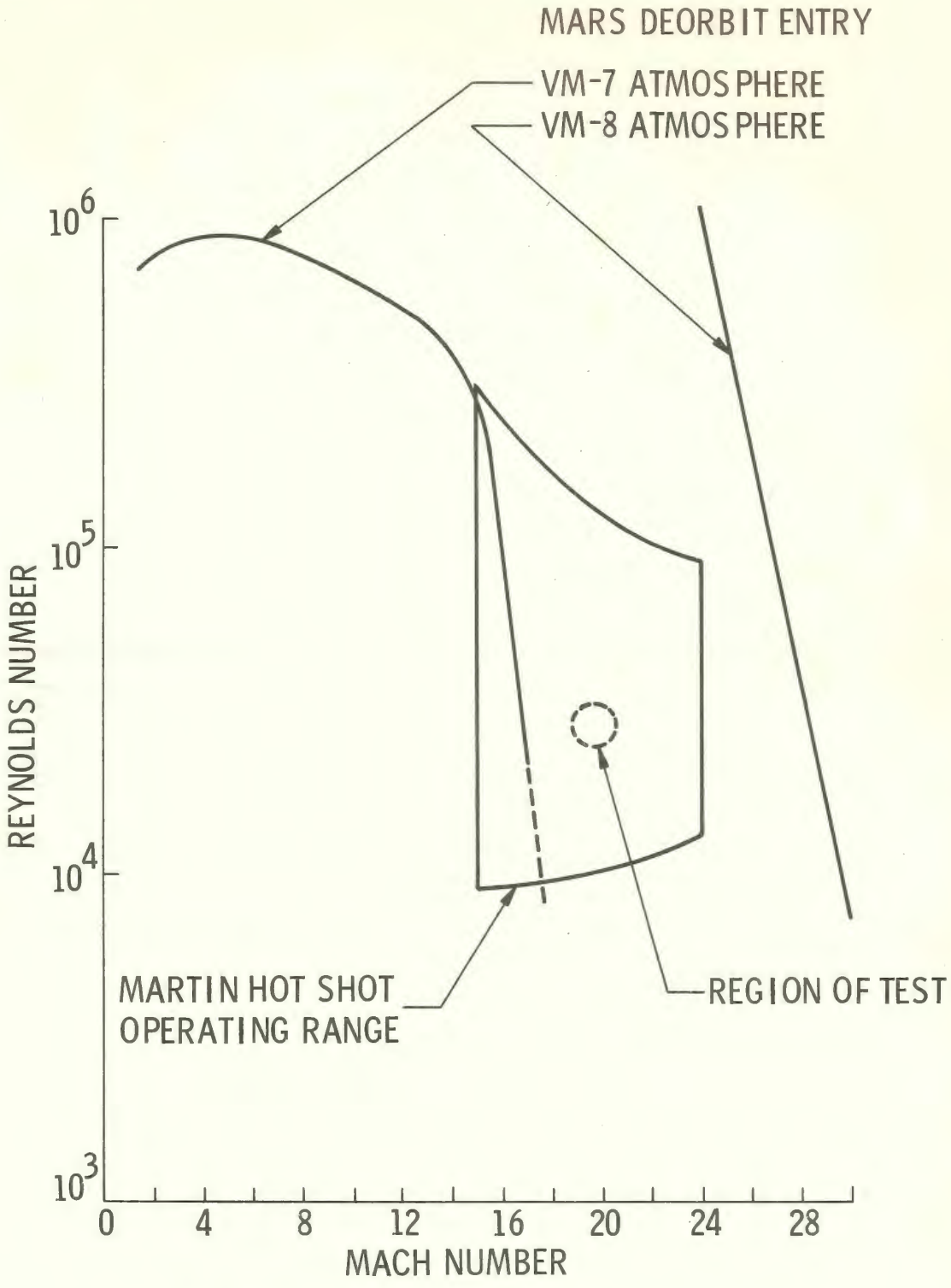


(a) REYNOLDS NUMBER VERSUS MACH NUMBER

**Figure 2. Trajectory Simulation.**

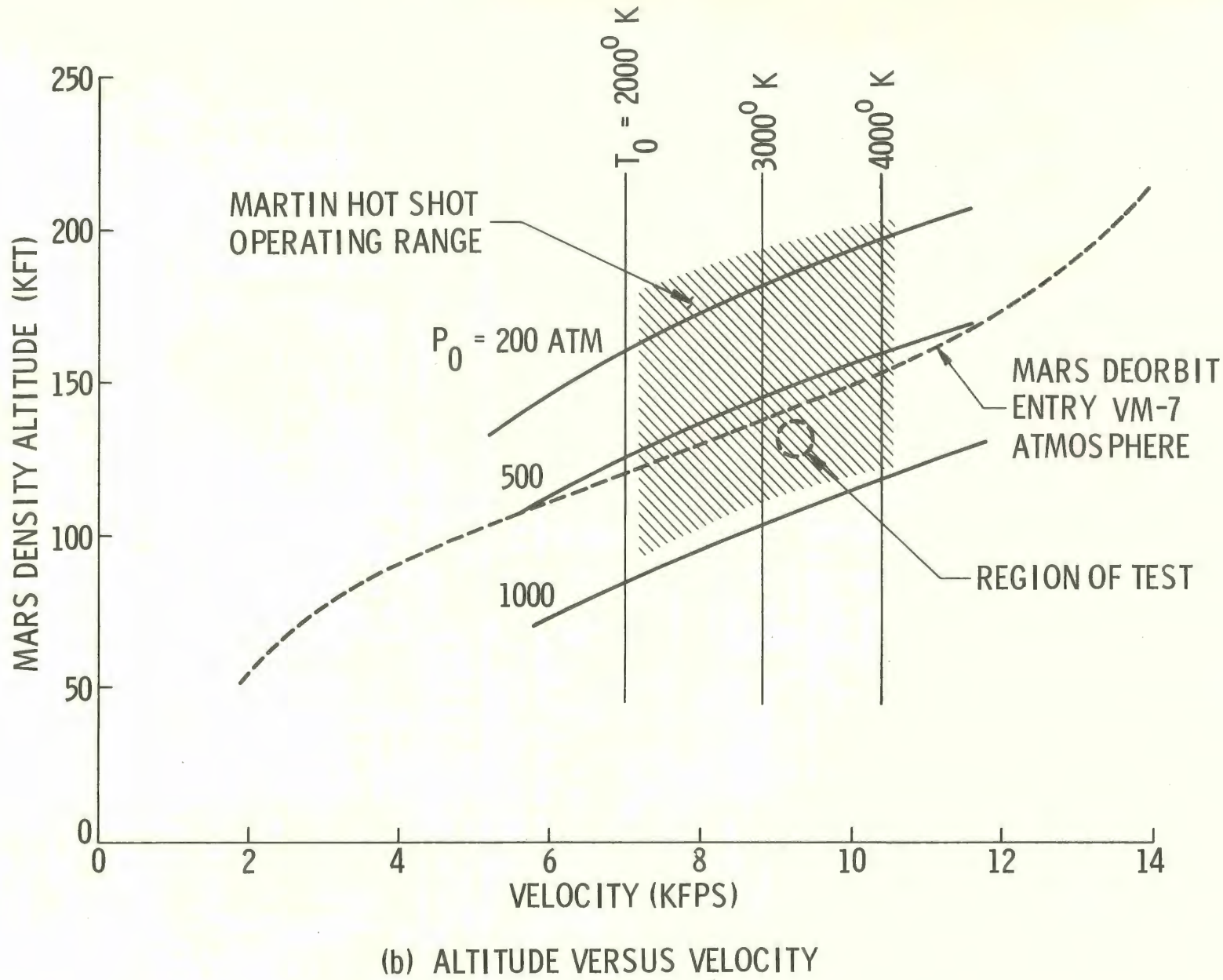


(b) ALTITUDE VERSUS VELOCITY

**Figure 2. Trajectory Simulation (Cont'd).**

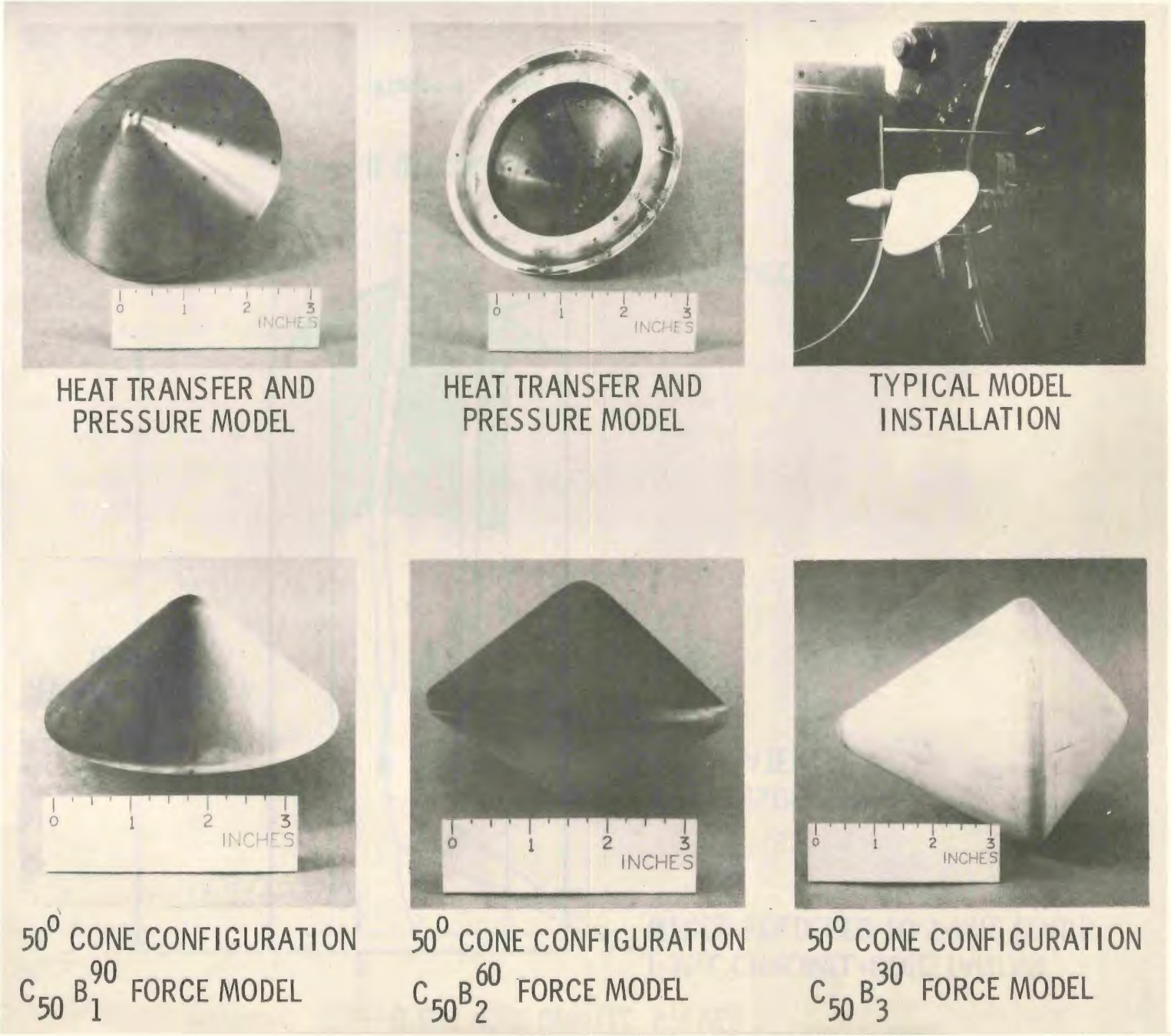


Figure 3. $50^{o}$ Cone Model Photographs.

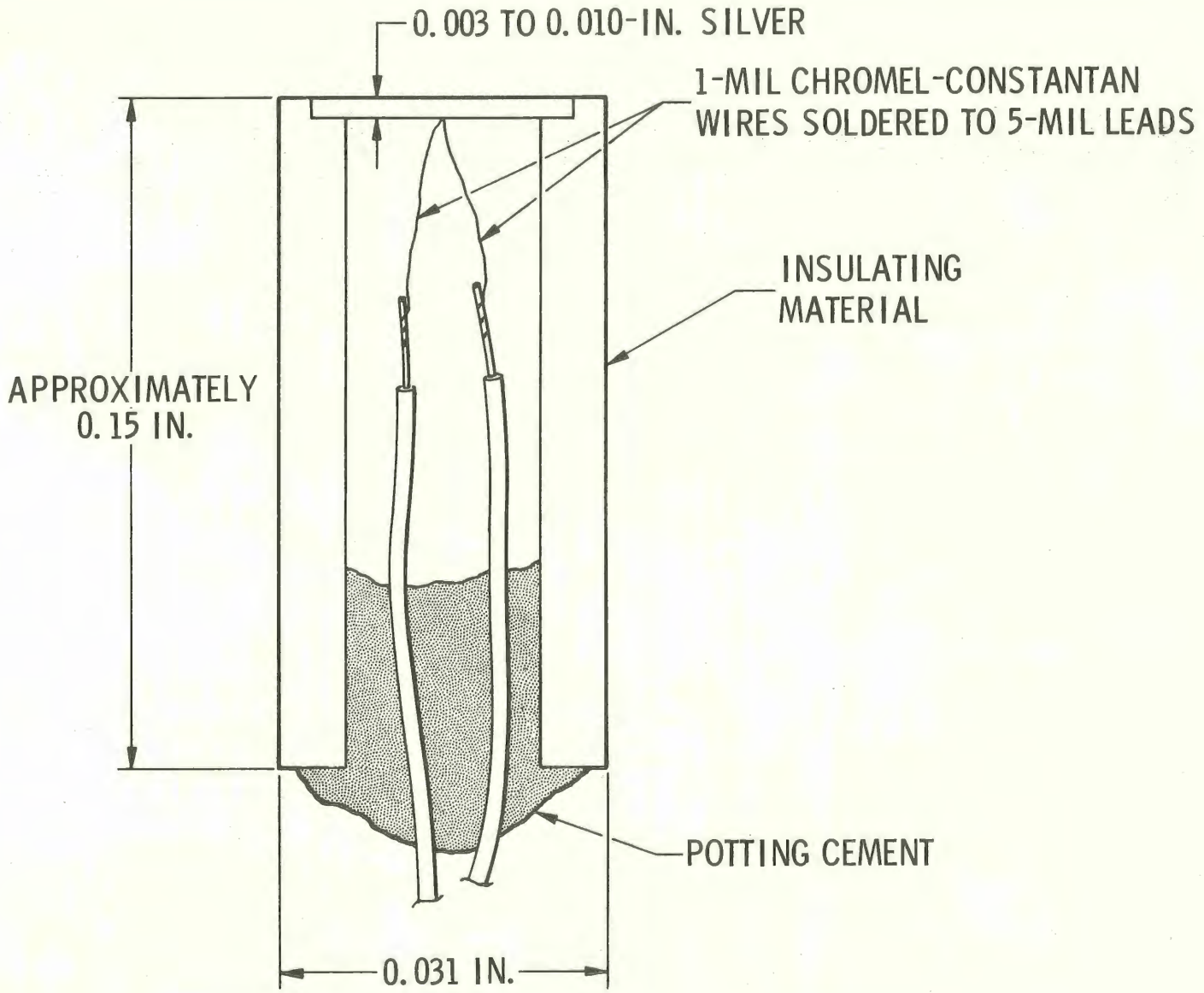


Figure 4. Heat Gage Details.

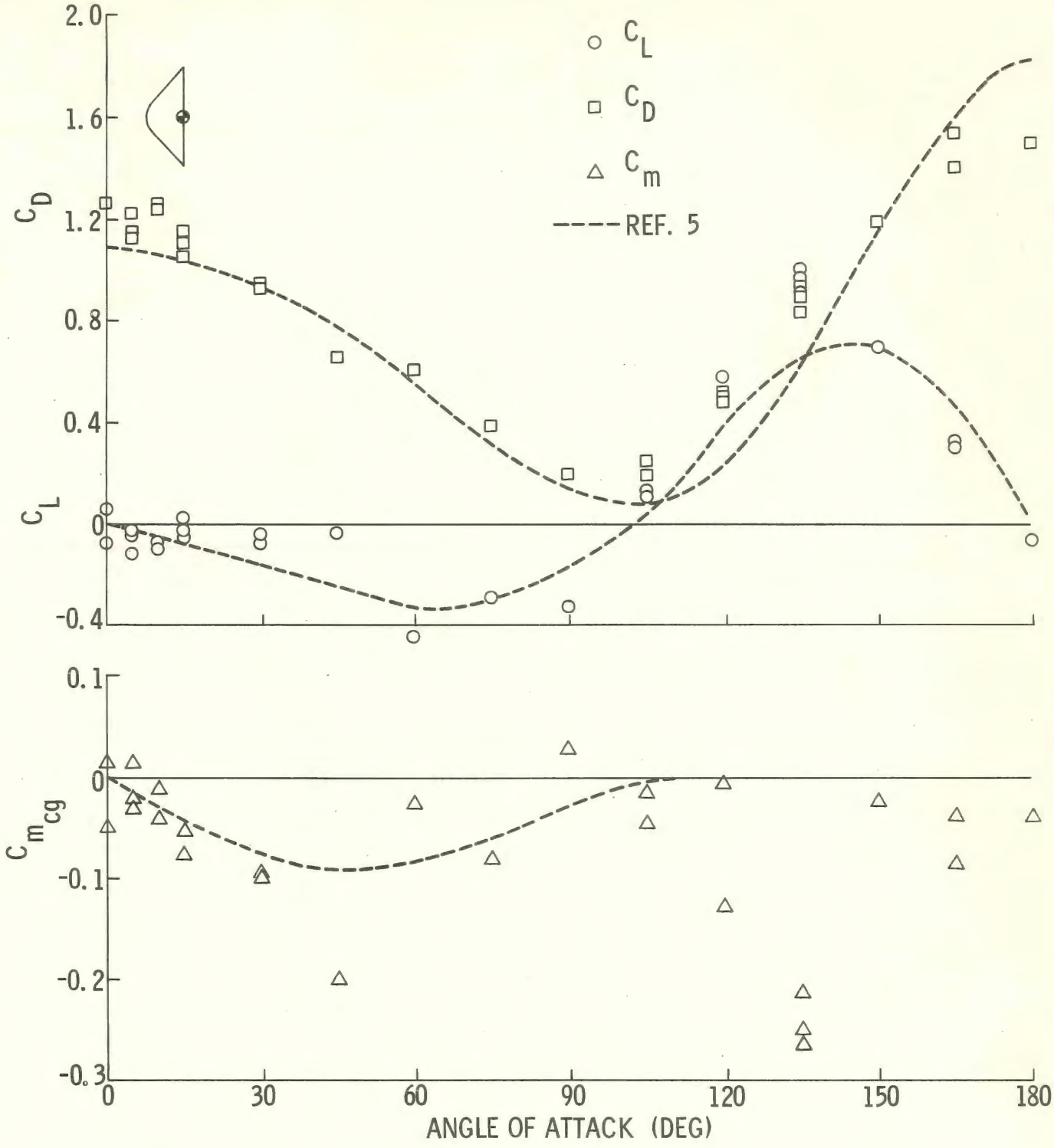


**Figure 5. Longitudinal Aerodynamic Characteristics Without Afterbody.**

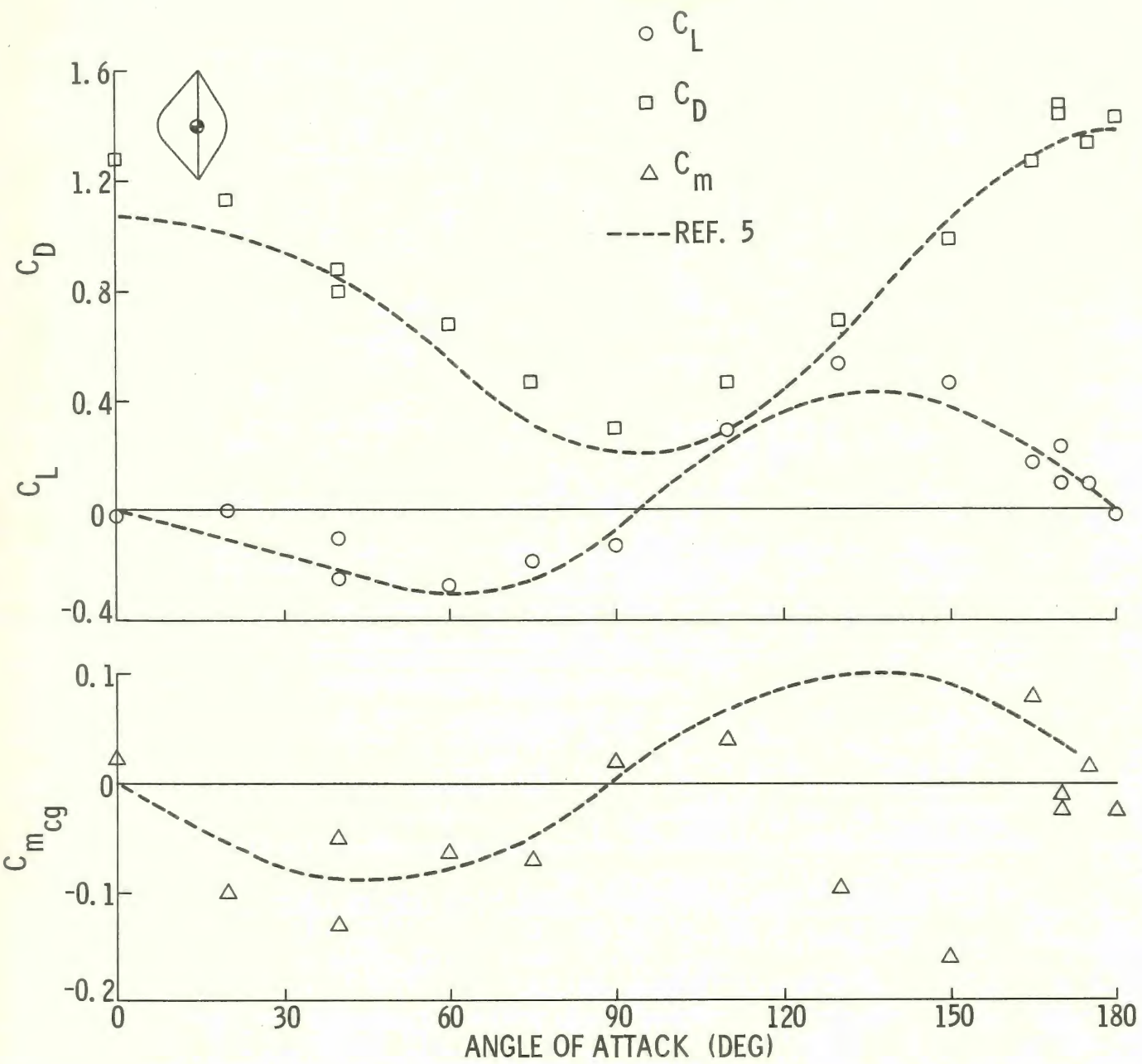


Figure 6. Longitudinal Aerodynamic Characteristics with 60° Semivertex Afterbody.

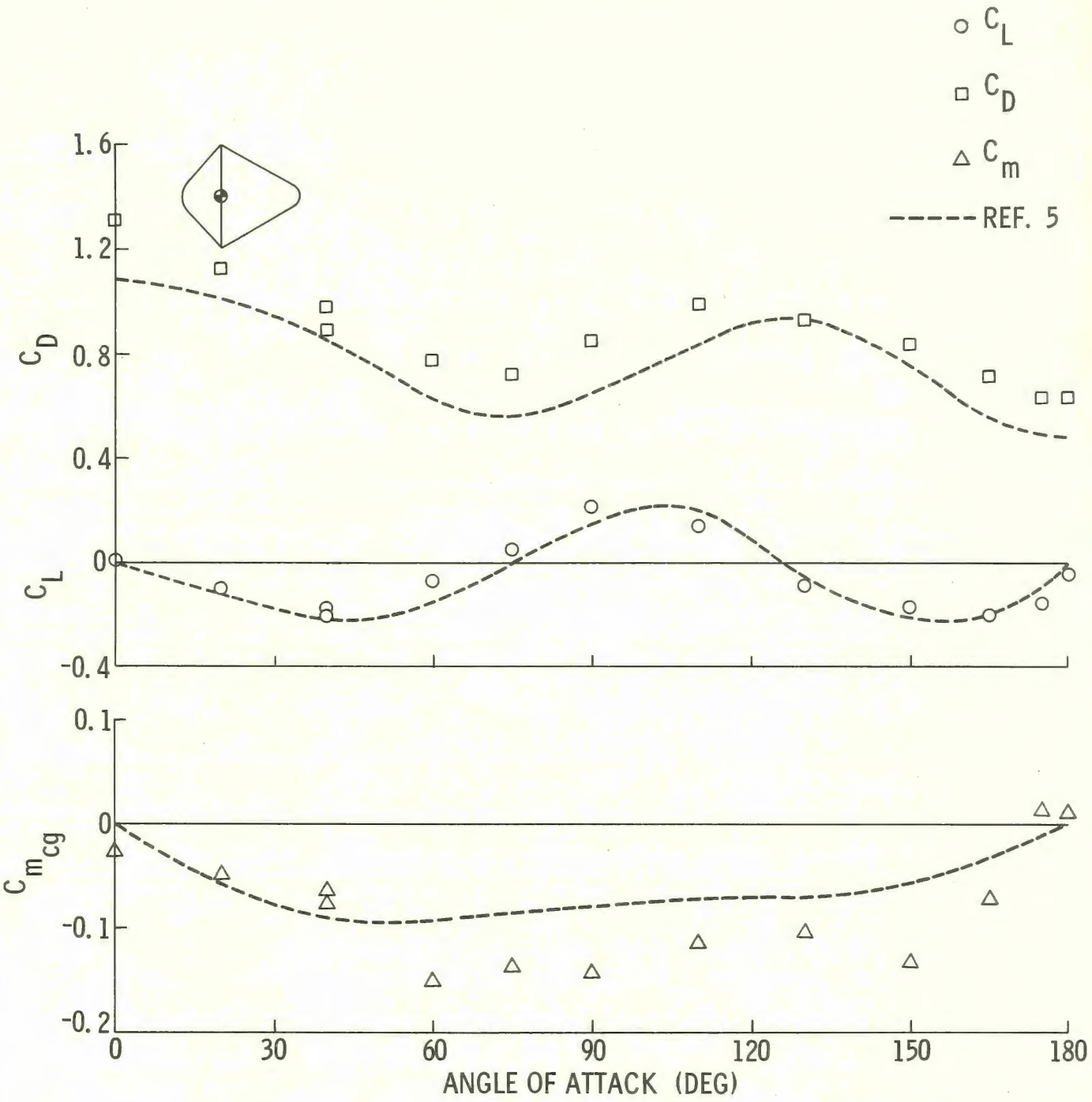


Figure 7. Longitudinal Aerodynamic Characteristics with $30^{\circ}$ Semivertex Afterbody.

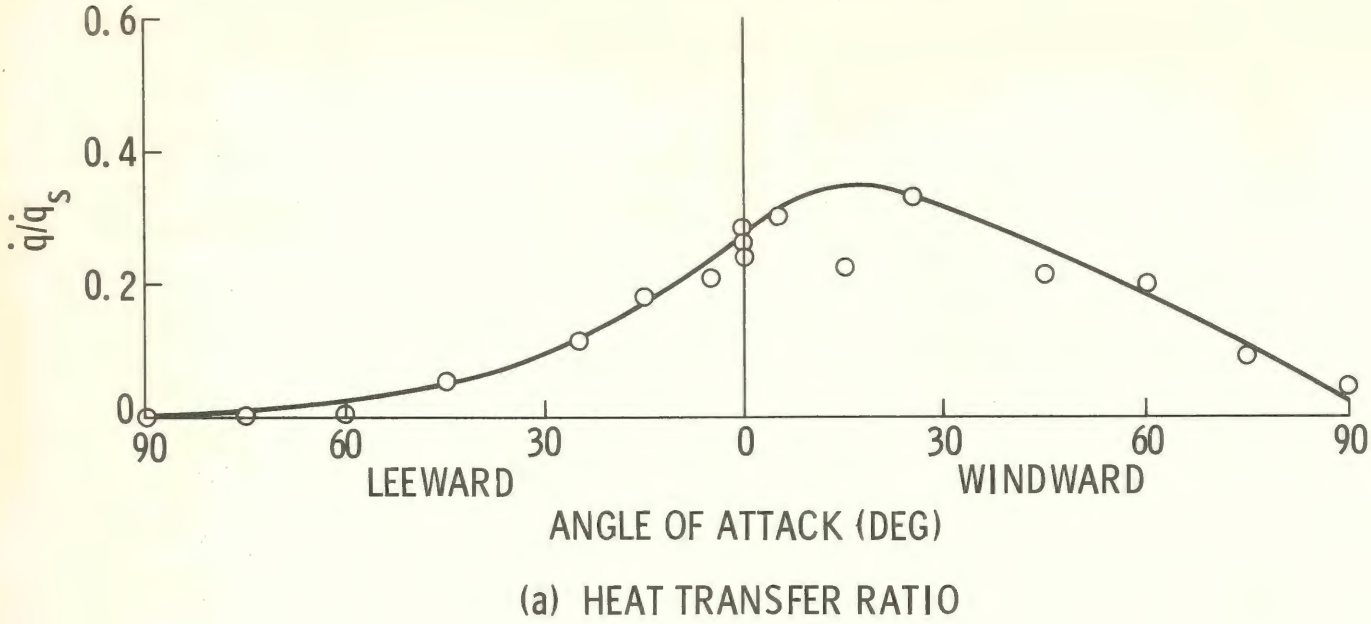


(a) HEAT TRANSFER RATIO

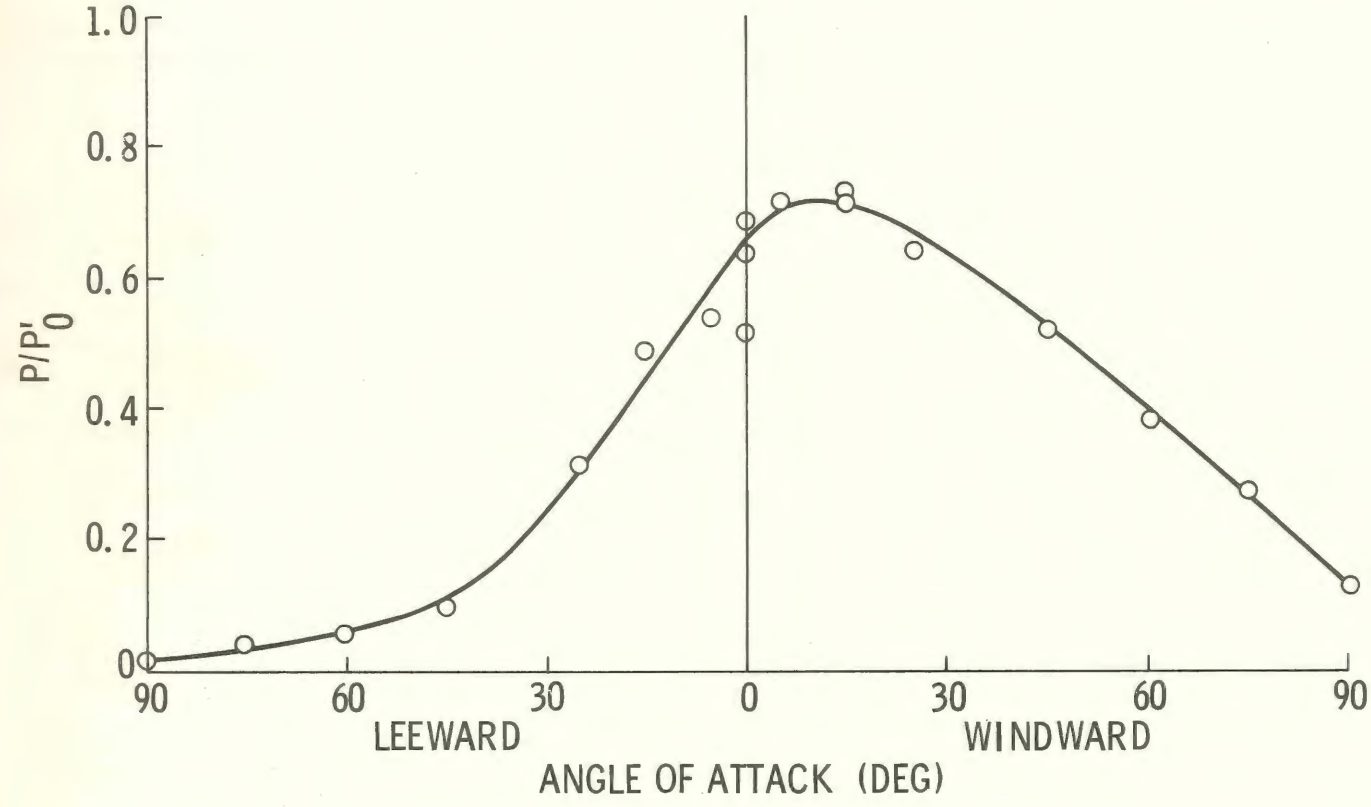


(b) PRESSURE RATIO

Figure 8. Variation of $\dot{q}/\dot{q}_s$ and $P/P'_0$ with Angle of Attack for Instrument Position II.

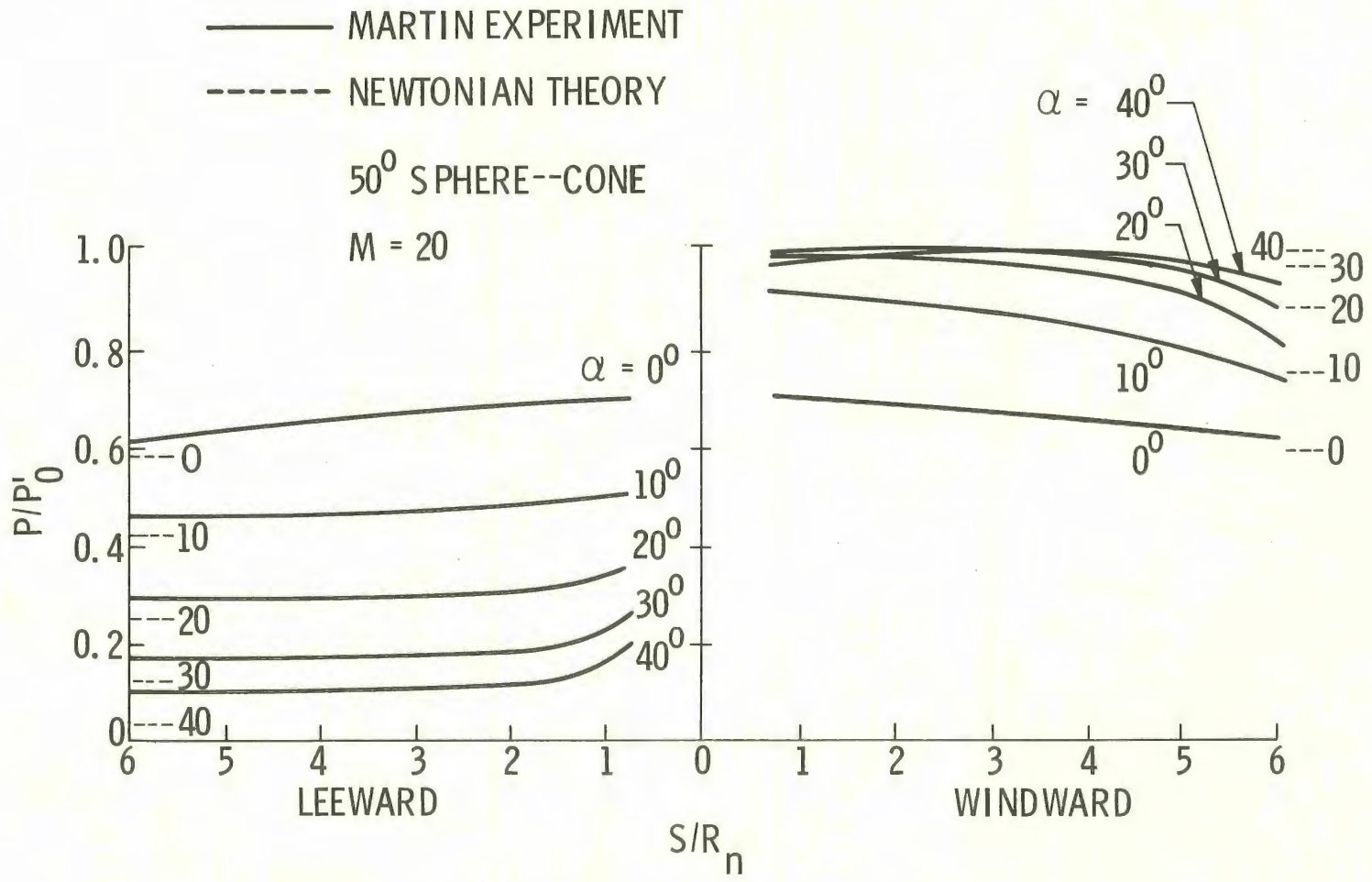


Figure 9. Pressure Distribution Along Windward and Leeward Meridians.

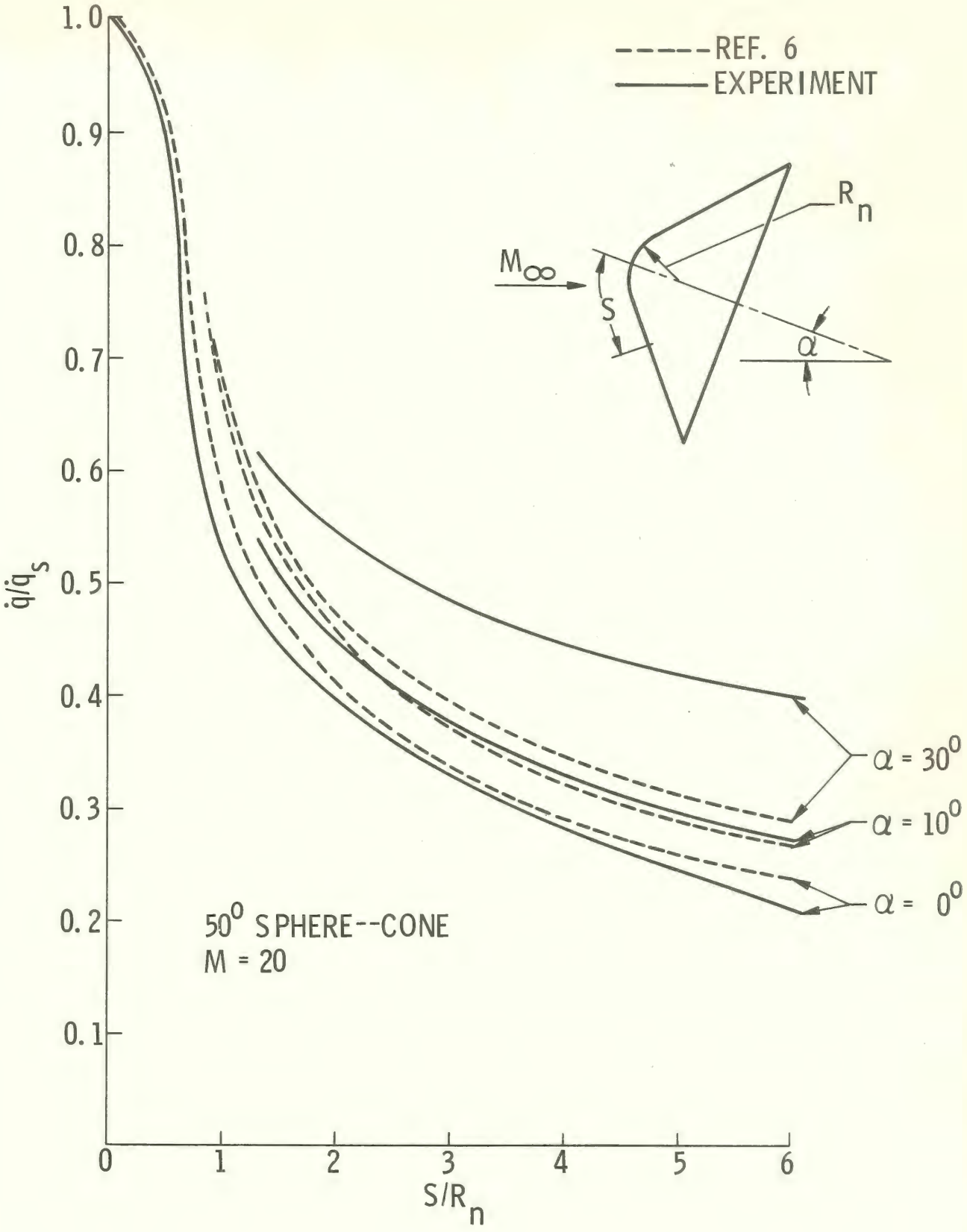


Figure 11. Heat Transfer Along Windward Meridian.

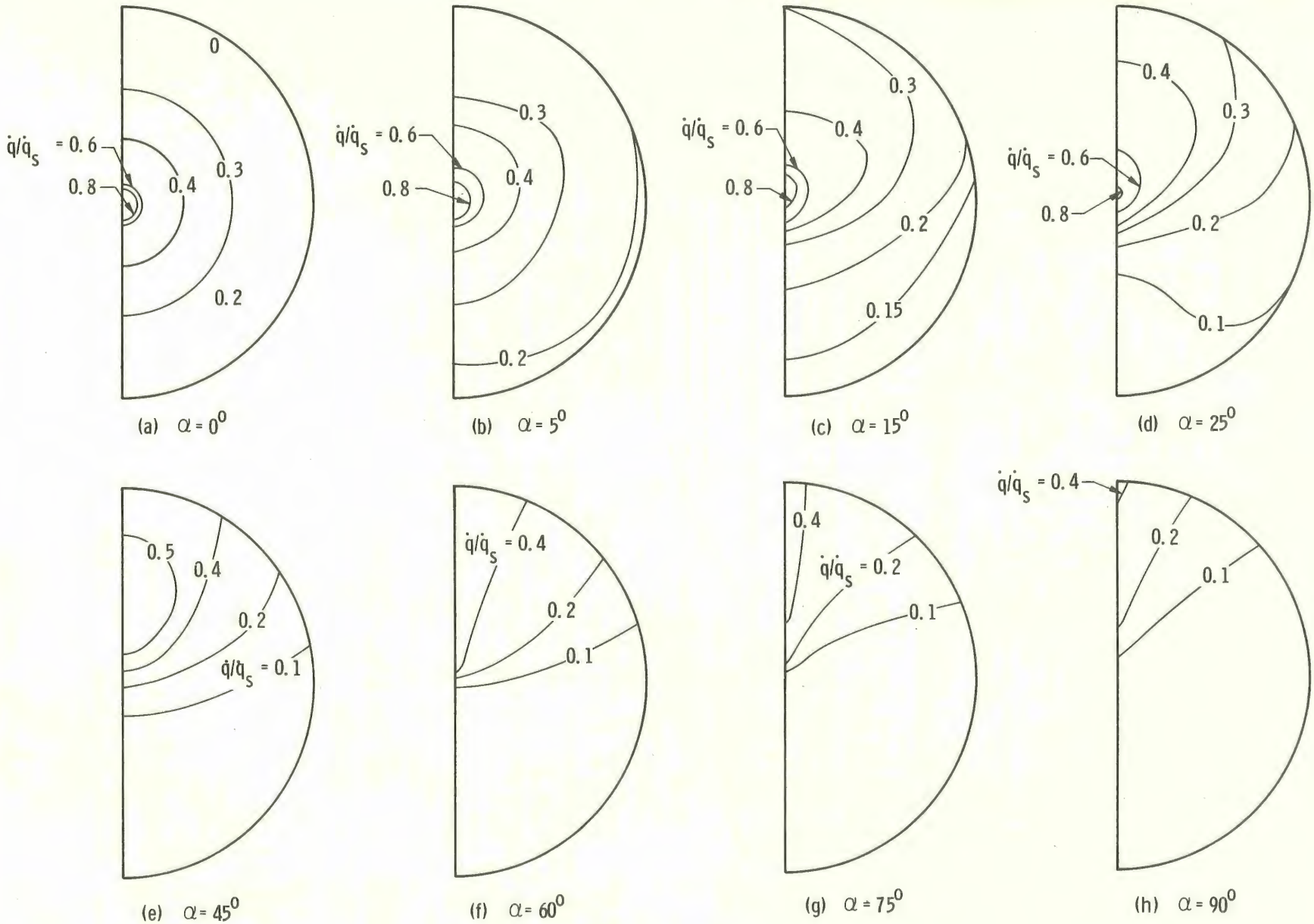


**Figure 12. Contours of Heat Transfer Ratio.**